

This is the accepted manuscript made available via CHORUS. The article has been published as:

Use of Stevens coefficients for the prediction of magnetic transitions in pseudobinary  $R_{1-x}R_x^{\prime}Al_2$  alloys: Application to  $Tm_{1-x}Tb_xAl_2$

Mahmud Khan, D. Paudyal, Ya. Mudryk, K. A. Gschneidner, Jr., and V. K. Pecharsky

Phys. Rev. B **83**, 134437 — Published 27 April 2011

DOI: [10.1103/PhysRevB.83.134437](https://doi.org/10.1103/PhysRevB.83.134437)

# **The use of Stevens' coefficients for the prediction of magnetic transitions in pseudobinary $R_{1-x}R'_xAl_2$ alloys: Application to $Tm_{1-x}Tb_xAl_2$**

Mahmud Khan, D. Paudyal, Ya. Mudryk

The Ames Laboratory U.S. Department of Energy, Iowa State University, Ames, Iowa  
50011-3020, USA

K. A. Gschneidner, Jr. and V. K. Pecharsky

The Ames Laboratory U.S. Department of Energy, Iowa State University, Ames, Iowa  
50011-3020, USA, and

Department of Materials Science and Engineering, Iowa State University, Ames, Iowa  
50011-2300, USA

Recent heat capacity and low field magnetic susceptibility measurements revealed unusual magnetic phenomena occurring in  $Er_{1-x}R_xAl_2$  systems (where  $R = Dy, Tb$ ) in the vicinity of a “magic” concentration of  $x = 0.25$ . Empirically, the reasons for such behavior were attributed to different shapes of the  $4f$  charge densities of the  $R^{3+}$  ions, which are represented by the opposite signs of the second order Stevens' factors. Here we show that by using both the signs and magnitudes of the second order Stevens' factors, magnetic transitions can be predicted in a broader range of pseudo binary  $R_{1-x}R'_xAl_2$  alloys where  $R$  and  $R'$  are rare earth metals that have opposite signs of second order Stevens' factors. The predictions have been verified using  $Tm_{1-x}Tb_xAl_2$  system as model

using x-ray diffraction, magnetic susceptibility and heat capacity measurements. First principles calculations have also been performed in order to explore the behavior of the density of states near the Fermi level.

PACS No's: 75.50.Cc, 75.10.Dg, 71.20.Lp, 71.20.Eh.

## Introduction

The fundamental magnetic properties of the  $RAI_2$  compounds, where R is a rare earth element, have continuously attracted attention of researchers for more than forty years.<sup>1,2,3,4,5</sup> Specifically the isostructural  $RAI_2$  compounds are well known for interesting properties including crystalline electric field effects<sup>5</sup> and low temperature ferromagnetism<sup>4,5</sup> that can be controlled by varying the rare earth component. Recent research results suggest that despite of broad experimental and theoretical investigations that have been already performed using these relatively simple  $MgCu_2$ -type Laves phases, some fascinating and new phenomena in the  $RAI_2$  compounds are yet to be discovered.

Most of the earlier studies explored the properties of the pure binary  $RAI_2$  compounds. Since the  $4f$  charge densities of the R atoms are significantly different from one another, unusual behaviors may be observed when the R atoms in the  $RAI_2$  alloys are partially replaced by a different R' atom to form pseudo binary  $R_{1-x}R'_xAl_2$  compounds. Such replacements have resulted in important discoveries such as zero net magnetic moment in ferromagnetic  $(Sm_{1-x}Gd_x)Al_2$ ,<sup>6</sup> large magnetocaloric effects in  $(Er_{1-x}Dy_x)Al_2$ ,<sup>7,8</sup> and exchange bias in  $Nd_{0.75}Ho_{0.25}Al_2$ .<sup>9</sup> In addition, exceptionally exciting discoveries were recently made in pseudo binary  $Er_{1-x}Dy_xAl_2$  and  $Er_{1-x}Tb_xAl_2$  alloys.<sup>10,11,12,13</sup>

Partial replacement of Er by Dy or Tb in  $Er_{1-x}Dy_xAl_2$  and  $Er_{1-x}Tb_xAl_2$ , respectively, causes the evolution of multiple magnetic ordering phenomena that behave unusually

with varying Dy and Tb concentration. The phenomena are represented by the appearance of first order peaks in the zero magnetic field heat capacities of the alloys.<sup>8,10,12</sup> The heat capacity peaks appear only in certain Er rich alloys in the series where the Tb and Dy concentrations center around  $x = 0.25$ . We note that the heat capacity peaks in  $\text{Er}_{1-x}\text{Dy}_x\text{Al}_2$  and  $\text{Er}_{1-x}\text{Tb}_x\text{Al}_2$  appear in the samples when the exchange interactions in the solvent (e.g.  $\text{Er}^{3+}$ ) are weaker than the same in the solute, which can be quantified by the de Gennes factor (de Gennes factors of  $\text{Er}^{3+}$ ,  $\text{Dy}^{3+}$  and  $\text{Tb}^{3+}$  are 0.162, 0.450, and 0.667, respectively).<sup>14</sup>

As the Tb and Dy concentration either reduces or exceeds the critical concentration of  $x = 0.25$ , the heat capacity peaks in  $\text{Er}_{1-x}\text{Dy}_x\text{Al}_2$  and  $\text{Er}_{1-x}\text{Tb}_x\text{Al}_2$  starts diminishing and finally disappear. It was proposed that the observed behavior is a result of the competition between the magnetoelastic and quadrupolar effects, which is caused by the modification of the magnetic structure due to Dy and Tb doping.<sup>10,11,12</sup> It was also suggested that the modification of the magnetic structure of the  $\text{Er}_{1-x}\text{Dy}_x\text{Al}_2$  and  $\text{Er}_{1-x}\text{Tb}_x\text{Al}_2$  systems was mainly caused by the  $4f$  charge densities of  $\text{Er}^{3+}$  being different from  $\text{Dy}^{3+}$  and  $\text{Tb}^{3+}$ .<sup>11,12</sup> The  $4f$  charge density of  $\text{Er}^{3+}$  is a prolate spheroid, whereas the  $4f$  charge densities of  $\text{Dy}^{3+}$  and  $\text{Tb}^{3+}$  are shaped as oblate spheroids, i.e. the sign of the second order Stevens' factor of  $\text{Er}^{3+}$  (4/45.35) is positive while the signs for  $\text{Dy}^{3+}$  (-2/9.35) and  $\text{Tb}^{3+}$  (-1/99) are negative.<sup>15</sup>

Although the heat capacities of  $\text{Er}_{1-x}\text{Dy}_x\text{Al}_2$  and  $\text{Er}_{1-x}\text{Tb}_x\text{Al}_2$  alloys exhibit a similar behavior, the first order like peaks in the  $\text{Er}_{1-x}\text{Tb}_x\text{Al}_2$  alloys are much weaker. The reason

for the weaker peaks in  $\text{Er}_{1-x}\text{Tb}_x\text{Al}_2$  was attributed to the smaller magnitude of the second order Stevens' factor for  $\text{Tb}^{3+}$  when compared to that for  $\text{Dy}^{3+}$ .<sup>12</sup> However, the magnitude of the second order Stevens' factors only seem to affect the heat capacity peaks and the ac susceptibility data. The magnetization verses temperature data of both  $\text{Er}_{1-x}\text{Dy}_x\text{Al}_2$  and  $\text{Er}_{1-x}\text{Tb}_x\text{Al}_2$  remain quite similar.<sup>11, 13</sup>

So far all of the reported pseudo binary  $\text{R}_{1-x}\text{R}'_x\text{Al}_2$  compounds, exhibiting the multiple magnetic ordering phenomena, contain Er. From the basic science point of view it is interesting to explore  $\text{R}_{1-x}\text{R}'_x\text{Al}_2$  compounds where R is a rare earth element with a positive signed second order Stevens' factor other than Er. If the aforementioned proposed reasons behind the observation of the multiple magnetic ordering phenomena are valid, then similar behavior should be observed in other  $\text{R}_{1-x}\text{R}'_x\text{Al}_2$  compounds containing rare earth elements with opposite signs of second order Stevens' factors besides Er. Therefore, in the current work we explore the magnetic and thermal properties of  $\text{Tm}_{1-x}\text{Tb}_x\text{Al}_2$  both experimentally and using first principles electronic structure calculations. We have selected Tm because its second order Stevens' factor is positive. Based on the reasoning described above we expect that multiple magnetic ordering should also be observed in  $\text{Tm}_{1-x}\text{Tb}_x\text{Al}_2$ . We also expect that the phenomenon should be centered around  $x = 0.25$ , since the de Gennes factor of  $\text{Tm}^{3+}$  (0.074) is lower than  $\text{Tb}^{3+}$  (0.667). The heat capacity peak is also expected to be weak as the magnitude of the second order Stevens' factor of  $\text{Tm}^{3+}$  (1/99) is much lower than that of  $\text{Er}^{3+}$  (4/43.5). We have also carried out first principles calculations in order to characterize the nature of

the density of states (DOS) near the Fermi level, as anomalies in DOS near Fermi level were observed in both  $\text{Er}_{1-x}\text{Dy}_x\text{Al}_2$  and  $\text{Er}_{1-x}\text{Tb}_x\text{Al}_2$ .<sup>13, 16</sup>

## Experimental details

The Tm and Tb metals used to prepare the  $\text{Tm}_{1-x}\text{Tb}_x\text{Al}_2$  ( $x = 0.25, 0.75, 1$ ) alloys were obtained from the Materials Preparation Center of the Ames Laboratory and were at least 99.8 at. % (99.98 wt %) pure with respect to all other elements in the periodic table.<sup>17</sup>

The Al metal of 5N purity was obtained from Alfa Aesar Inc. Polycrystalline buttons of  $\text{Tm}_{1-x}\text{Tb}_x\text{Al}_2$  alloys weighing approximately 5g each were prepared by conventional arc melting technique in an argon atmosphere. The alloys melt congruently and therefore, annealing was not necessary. To check the phase purity and identify the crystal structure of the samples, room temperature x-ray powder diffraction (XRD) was performed on a PANAnalytical powder diffractometer employing monochromatic  $\text{Cu K}\alpha_1$  radiation.

Temperature dependent XRD measurements were performed on a Rigaku TTRAX rotating anode powder diffractometer employing  $\text{Mo K}\alpha$  radiation.<sup>18</sup> The diffractometer was equipped with a continuous flow  $^4\text{He}$  cryostat controlling the temperature of a sample, which was prepared and mounted on a copper sample holder as described in Ref.19. The lattice parameters were determined by performing Reitveld refinement using LHPM-RIETICA.<sup>20</sup> The room temperature XRD data along with the refinement results of  $\text{Tm}_{0.75}\text{Tb}_{0.25}\text{Al}_2$  are shown in Fig. 1. The alloys are found to be pure and no secondary phases are observed in the XRD patterns. The  $\text{Tm}_{1-x}\text{Tb}_x\text{Al}_2$  alloys crystallize in the

MgCu<sub>2</sub> type cubic Laves phase structure with the following lattice parameters at room temperature:  $a = 7.7974 \text{ \AA}$  ( $x = 0.25$ ),  $a = 7.8435 \text{ \AA}$  ( $x = 0.75$ ) and  $a = 7.8666 \text{ \AA}$  ( $x = 1$ ). The lattice parameter for pure TmAl<sub>2</sub> (7.7757  $\text{\AA}$ ) was taken from the report of Harris et al.<sup>21</sup> As shown in the inset of Fig. 1, the lattice parameters depend linearly on the Tb concentration ( $x$ ). Assuming that Vegard's law holds (which is reasonable considering that the structure is cubic and that the Tm-Tb solid solution is nearly ideal), this suggests that the concentrations of our samples are close to the targeted concentration. The linear dependence of lattice parameters on the concentration of rare earth metals is also observed in the pseudo-binary Tb<sub>1-x</sub>Dy<sub>x</sub>Al<sub>2</sub> alloys.<sup>22</sup> The increase of the lattice parameters with increasing Tb concentration can be attributed to the larger ionic radius of Tb<sup>3+</sup> compared to that of Tm<sup>3+</sup>. The ac and dc magnetic measurements were conducted in a Superconducting Quantum Interference Device (SQUID) magnetometer MPMS XL-7 made by Quantum Design Inc. The measurements were performed in the temperature range of 2 – 300 K and in applied magnetic fields of up to 7 T. A homemade adiabatic heat-pulse calorimeter was used to conduct the heat capacity measurements.<sup>23</sup> The measurements were performed in the temperature range from ~2 to 350 K in a zero magnetic field and in applied magnetic fields up to 10 kOe.

## Results and discussions

### Tm<sub>0.75</sub>Tb<sub>0.25</sub>Al<sub>2</sub>

Figure 2 shows the dc magnetization,  $M(T)$ , of Tm<sub>0.75</sub>Tb<sub>0.25</sub>Al<sub>2</sub> measured as a function of temperature in a magnetic field of 100 Oe. Before measuring the zero field cooled (ZFC)



data, the sample was cooled from 300 K to 2 K in a zero magnetic field. When the temperature reached 2 K, a magnetic field of 100 Oe was applied, and the ZFC  $M(T)$  curve was recorded as a function of increasing temperature. The field cooled cooling (FCC) curve was measured while sweeping down the temperature from 300 K to 2 K. The field cooled warming (FCW) curve was obtained in a similar way to that of the ZFC curve with the exception that the sample was cooled down in the presence of a magnetic field of 100 Oe.

As shown in Fig. 2, the ZFC magnetization of  $Tm_{0.75}Tb_{0.25}Al_2$  initially decreases with increasing temperature until  $\sim 6$  K, and then sharply increases between 6 and 7 K. After this temperature the magnetization drops gradually. Around 21 K the sharp drop of magnetization represents the transition from the ferromagnetic to the paramagnetic state. The ZFC, FCC and FCW  $M(T)$  curves are identical between 300 K and 21 K, but below 21 K thermomagnetic irreversibility is observed. This thermomagnetic irreversibility can be clearly seen in the inset (a) of Fig. 1. Noticeable thermal hysteresis between the  $M(T)$  curves obtained while cooling and heating suggest that the transition observed near 7 K is a first order phase transition. From the derivative of the  $M(T)$  data, as shown in the inset (b) of Fig. 2, the low temperature transitions on cooling and heating occur at 6.8 K and 7.8 K, respectively, and  $T_C$  is 22 K.

Figure 3 shows the ZFC, FCC and FCW  $M(T)$  data of  $Tm_{0.75}Tb_{0.25}Al_2$  measured in a magnetic field of 1000 Oe. The inset shows the temperature dependence of the inverse susceptibility ( $H/M$ ) of the sample. The low temperature anomaly at  $\sim 7$  K observed in

the  $M(T)$  data obtained at 100 Oe is also apparent in the  $M(T)$  data collected at 1000 Oe, as shown in Fig. 3. However, the thermomagnetic irreversible behavior observed below 21 K in the 100 Oe  $M(T)$  data is not seen in the 1000 Oe  $M(T)$  data. Also the thermal hysteresis in the vicinity of the low temperature transition decreases significantly when a 1000 Oe field is applied. Above  $T_C$ , the inverse susceptibility follows the Curie-Weiss behavior. The effective magnetic moment,  $p_{eff}$ , and the paramagnetic Weiss temperature,  $\Theta_p$ , calculated from  $H/M$  vs.  $T$  data are  $8.03 \mu_B / R^{3+}$  and 24 K, respectively. The expected  $p_{eff}$ , which is obtained from the relation  $g\sqrt{J(J+1)}$  ( $g$  is the gyromagnetic factor, and  $J$  is the total angular momentum quantum number), for a mixture of  $0.75\text{Tm} + 0.25\text{Tb}$  noninteracting trivalent ions is  $8.16 \mu_B$ . This value is in good agreement with the experiment.

Figure 4 shows the field dependence of magnetization,  $M(H)$ , of  $\text{Tm}_{0.75}\text{Tb}_{0.25}\text{Al}_2$  measured at 2 K. The magnetic moment nearly saturates in 70 kOe magnetic field. The saturation moment was estimated by plotting  $M$  as a function of  $1/H$  followed by extrapolation to  $1/H = 0$ . The estimated value of the saturation moment of  $\text{Tm}_{0.75}\text{Tb}_{0.25}\text{Al}_2$  is  $6.76 \mu_B$ , which is notably smaller than the expected moment ( $m = gJ$ ) of  $7.5 \mu_B$ . The mismatch in the expected and observed saturation moment most probably arises from the crystalline electric field effects. “Such mismatches due to crystalline electric fields are also observed in pure  $\text{TmAl}_2$ <sup>24</sup> and in pseudo-binary  $\text{Er}_{1-x}\text{Dy}_x\text{Al}_2$  and  $\text{Er}_{1-x}\text{Tb}_x\text{Al}_2$  alloys.”<sup>11, 13</sup> As shown in the inset of Fig. 4, nearly negligible hysteresis is observed in the  $M(H)$  data of  $\text{Tm}_{0.75}\text{Tb}_{0.25}\text{Al}_2$ .

The temperature variations of the real and imaginary components of the ac susceptibility of  $\text{Tm}_{0.75}\text{Tb}_{0.25}\text{Al}_2$  obtained in zero dc magnetic field are shown in Figs. 5a and 5b, respectively. The measurements were performed on heating in an ac field ( $H_{\text{ac}}$ ) of 5 Oe, and at frequencies of 1 Hz, 10 Hz, 100 Hz, and 1000 Hz. As shown in Fig. 5a, the real component of the ac susceptibility,  $\chi'$ , increases with increasing temperature with a peak at  $\sim 7$  K. We believe that this is due to the first order like transition observed in the  $M(T)$  data of the alloy (see Fig. 2). The peak around 7 K diminishes with the increasing frequency (see the inset of Fig. 5a for clarity). Above 7 K,  $\chi'$  increases with increasing temperature until it drops sharply at  $T_C$ . A weak frequency dependence is also observed in the  $\chi'$  data below  $T_C$ . The  $\chi''$  data (Fig. 5b) measured at a frequency of 1 Hz shows a small rounded peak around 3 K, a sharp peak at 7 K, and a sharp drop in  $\chi''$  at  $T_C \approx 22$  K. The rounded peak at 3 K disappears for frequencies equal to and greater than 10 Hz. It is noted that the anomaly represented by the rounded peak at 3 K is not observed in any other measurements. Similar rounded peak is also observed in the  $\chi''$  data of  $\text{Er}_{0.75}\text{Tb}_{0.25}\text{Al}_2$  but not in the  $\chi''$  data of  $\text{Er}_{0.75}\text{Dy}_{0.25}\text{Al}_2$ .<sup>11, 13</sup> The sharp peak at 7 K in the  $\chi''$  data diminishes with increasing frequency, but a weak anomaly is still observed around this temperature even at 1000 Hz.

As expected, the low temperature ( $\sim 7$  K) anomaly observed in the ac susceptibility data of  $\text{Tm}_{0.75}\text{Tb}_{0.25}\text{Al}_2$  is similar to  $\text{Er}_{0.75}\text{Tb}_{0.25}\text{Al}_2$ <sup>13</sup> but it is much weaker than in

$\text{Er}_{0.75}\text{Dy}_{0.25}\text{Al}_2$ .<sup>11</sup> The reason of such behaviour is attributed to the smaller magnitudes of second order Stevens' factors of  $\text{Tm}^{3+}$  and  $\text{Tb}^{3+}$ .

As mentioned earlier, the central characteristic of the multiple magnetic ordering phenomena were revealed in the heat capacity measurements<sup>10, 12</sup> (i.e., the existence of sharp first order peaks in the heat capacity in the vicinity of the transition). To explore if such peaks exist in  $\text{Tm}_{0.75}\text{Tb}_{0.25}\text{Al}_2$  alloy, we have performed heat capacity measurements. Figure 6 shows the heat capacity,  $C_P$ , of  $\text{Tm}_{0.75}\text{Tb}_{0.25}\text{Al}_2$  measured as a function of temperature in zero magnetic field. The figure also shows the 100 Oe field  $M(T)$  data of the same alloy. Initially with increasing temperature  $C_P$  increases linearly until 7 K where change in slope is observed. As shown in the inset of Fig. 7, it appears to be a peak-like anomaly. It is clear in the figure that the change in slope in  $C_P$  and the anomaly in  $M(T)$  occur at the same temperature. With a further increase of temperature,  $C_P$  increases linearly until it drops at  $T_C$ . Figure 7 shows the  $C_P$  as a function of temperature measured in different magnetic fields. The low temperature anomaly is easily suppressed by the application of weak magnetic fields (see inset of Fig. 7).

At this point it is worth noting that the observed behaviors correlate very well with the predictions made.<sup>12</sup> As predicted, the unusual first order like magnetic transitions were expected to be present in  $\text{Tm}_{1-x}\text{Tb}_x\text{Al}_2$  alloy ( $x$  centered on 0.25) due to the fact that the second order Stevens' factors of  $\text{Tm}^{3+}$  and  $\text{Tb}^{3+}$  are opposite. However, since the magnitudes of the Stevens' factors are small ( $1/99$  for  $\text{Tm}^{3+}$  and  $-1/99$  for  $\text{Tb}^{3+}$ ), the heat capacity peak is expected to be weak in  $\text{Tm}_{1-x}\text{Tb}_x\text{Al}_2$ . Based on the suggestion made

earlier in reference 12, the behavior of the first order anomaly in the heat capacity may partly be attributed also to the variability of the easy magnetization direction of the  $R_{1-x}R'_xAl_2$  system as a function of concentration. If for both  $x = 0$  and  $1$ , the easy magnetization direction is the same, then there is no driving force for a spin reorientation transition in the pseudo binary alloy resulting in a weak anomaly in the heat capacity. This is indeed the case for the  $Tm_{0.75}Tb_{0.25}Al_2$  alloy, as both  $TmAl_2$  and  $TbAl_2$  have easy magnetization axis along the  $\langle 111 \rangle$  direction.

Temperature dependent x-ray diffraction (XRD) measurements show that no change in the crystal structure takes place in the vicinity of the first order anomalies in  $Er_{0.75}Tb_{0.25}Al_2$ <sup>13</sup> and  $Er_{0.75}Dy_{0.25}Al_2$ .<sup>11</sup> It is also expected that no structural transition accompanies the first order like transition near 7 K in  $Tm_{0.75}Tb_{0.25}Al_2$ . However, to confirm such is the case we have performed temperature dependent XRD measurements on the  $Tm_{0.75}Tb_{0.25}Al_2$  sample. As expected, we have not observed any structural change in the alloy. The lattice parameters are plotted as a function of temperature in Fig. 8. Similar to  $Er_{0.75}Tb_{0.25}Al_2$  and  $Er_{0.75}Dy_{0.25}Al_2$ , the lattice constant decreases smoothly with decreasing temperature until  $T_C$ , below which a slight deviation is observed.

### **$Tm_{0.25}Tb_{0.75}Al_2$ and $TbAl_2$**

The  $M(T)$  data of  $Tm_{0.25}Tb_{0.75}Al_2$  measured in a magnetic field of 100 Oe are shown in Fig. 9. The upper inset of Fig. 9 shows the  $M(T)$  data obtained under same condition for  $TbAl_2$ , and the lower inset shows the dependence of  $T_C$  on Tb concentration ( $x$ ). The only

transition observed in the  $M(T)$  data of  $\text{Tm}_{0.25}\text{Tb}_{0.75}\text{Al}_2$  is the ferromagnetic transition at  $T_C \cong 83$  K. In  $\text{TbAl}_2$  as well, the only transition observed is at  $T_C \cong 111$  K. The low temperature anomaly observed in the  $M(T)$  data of the  $\text{Tm}_{0.75}\text{Tb}_{0.25}\text{Al}_2$  alloy is no longer observed in either  $\text{Tm}_{0.25}\text{Tb}_{0.75}\text{Al}_2$  or in  $\text{TbAl}_2$ . As shown in the lower inset of Fig. 9,  $T_C$  increases linearly with increasing Tb concentration.  $T_C = 3.4$  K of pure  $\text{TmAl}_2$  was taken from Ref. 25. The  $M(T)$  data of  $\text{Tm}_{0.25}\text{Tb}_{0.75}\text{Al}_2$  measured at 1000 Oe are also significantly different than those measured for  $\text{Tm}_{0.75}\text{Tb}_{0.25}\text{Al}_2$  (see Fig. 3). The only transition observed in Fig. 10 is the ferromagnetic transition at  $T_C$ . The  $M(T)$  data of  $\text{TbAl}_2$  obtained at 1000 Oe (not shown) also shows similar behavior. As shown in the inset of Fig. 10, the inverse susceptibility of  $\text{Tm}_{0.25}\text{Tb}_{0.75}\text{Al}_2$  follows the Curie-Weiss behavior above  $T_C$ . The  $p_{\text{eff}}$  and  $\Theta_P$ , calculated from  $H/M$  vs.  $T$  data are  $9.4 \mu_B / R^{3+}$  and 84 K, respectively. The expected  $p_{\text{eff}}$  for a mixture of  $0.25\text{Tm} + 0.75\text{Tb}$  noninteracting trivalent ions is  $9.23 \mu_B$ , which is comparable with the experimental value. The  $p_{\text{eff}}$  and  $\Theta_P$ , calculated for  $\text{TbAl}_2$  are  $9.75 \mu_B$  and 115 K, respectively. For  $\text{Tb}^{3+}$  the expected  $p_{\text{eff}}$  is  $9.72 \mu_B$ , which is in good agreement with the experimental value. The saturation moments of  $\text{Tm}_{0.25}\text{Tb}_{0.75}\text{Al}_2$  and  $\text{TbAl}_2$  at 2 K are  $8.67 \mu_B$  ( $8.5 \mu_B$  expected theoretical value) and  $8.96 \mu_B$  ( $9 \mu_B$  expected theoretical value), respectively.

Figure 11 shows the ac magnetic susceptibilities of  $\text{Tm}_{0.25}\text{Tb}_{0.75}\text{Al}_2$ . The only transition observed in the  $\chi'$  data is a sharp drop at  $T_C$ . The low temperature anomalies observed in the  $\chi'$  and  $\chi''$  data of  $\text{Tm}_{0.75}\text{Tb}_{0.25}\text{Al}_2$  (see Fig. 5) are not observed in Fig. 11. Below  $T_C$ , a frequency dependence is observed in the  $\chi'$  data. Although not shown, the  $\chi'$  and  $\chi''$  data

of  $\text{TbAl}_2$  are quite similar to those of  $\text{Tm}_{0.75}\text{Tb}_{0.25}\text{Al}_2$  and no low temperature anomalies are observed.

Figure 12 shows the  $C_P(T)$  data of  $\text{Tm}_{0.25}\text{Tb}_{0.75}\text{Al}_2$ . With increasing temperature  $C_P$  of  $\text{Tm}_{0.25}\text{Tb}_{0.75}\text{Al}_2$  increases until it drops at  $T_C$ . Besides this drop in  $T_C$  no other anomalies is observed in the  $C_P$  data of  $\text{Tm}_{0.25}\text{Tb}_{0.75}\text{Al}_2$ . The  $C_P$  of  $\text{TbAl}_2$  shows a similar behavior.

### First Principles Calculations

In order to further understand the magnetism of  $\text{Tm}_{0.75}\text{Tb}_{0.25}\text{Al}_2$  and  $\text{Tm}_{0.25}\text{Tb}_{0.75}\text{Al}_2$ , first principles electronic structure calculations have been performed using the tight binding linear muffin tin orbital (TB-LMTO) method.<sup>26</sup> The local spin density approximation (LSDA) and generalized gradient approximation (GGA) have been employed considering  $4f$  electrons of Tm and Tb as core electrons. In order to reduce the possible imprecision of the atomic sphere approximation and to consider the full potentials, we have also used the full potential linear augmented plane-wave (FP-LAPW) method. The GGA, including Hubbard U (GGA+U) approach,<sup>27, 28</sup> has also been applied. In order to properly position the occupied and unoccupied  $4f$  energy levels in the electronic structure calculations of both  $\text{Tm}_{0.75}\text{Tb}_{0.25}\text{Al}_2$  and  $\text{Tm}_{0.25}\text{Tb}_{0.75}\text{Al}_2$ , we have used Hubbard  $U = 5.7$  eV and 3.4 eV for Tb and Tm, respectively. These values were mapped from the occupied ground state (determined from photoemission spectroscopy) and the unoccupied (determined from bremsstrahlung isochromatic spectroscopy) energy levels of Tb and Tm given in reference 29. The calculations with higher values of  $U$  shift

the unoccupied  $4f$  energy levels to higher energy side as expected. The effect of spin orbit interactions has also been taken into account.

The electronic structure calculations for  $\text{Tm}_{0.75}\text{Tb}_{0.25}\text{Al}_2$  and  $\text{Tm}_{0.25}\text{Tb}_{0.75}\text{Al}_2$  were performed by using the same unit cell volume but changing the cubic symmetry to  $P1$  symmetry and placing Tm and Tb atoms to match the stoichiometry. Since no superstructure peaks indicating possible ordering of Tm and Tb atoms were observed on the x-ray patterns of these alloys, out of eight rare earth sites ( $0\ 0\ 0$ ,  $\frac{1}{2}\ 0\ \frac{1}{2}$ ,  $\frac{1}{2}\ \frac{1}{2}\ 0$ ,  $0\ \frac{1}{2}\ \frac{1}{2}$ ,  $\frac{3}{4}\ \frac{1}{4}\ \frac{3}{4}$ ,  $\frac{1}{4}\ \frac{1}{4}\ \frac{1}{4}$ ,  $\frac{3}{4}\ \frac{3}{4}\ \frac{1}{4}$ ,  $\frac{1}{4}\ \frac{3}{4}\ \frac{3}{4}$ ) in the  $P1$  structure six for Tm and two for Tb atoms for  $\text{Tm}_{0.75}\text{Tb}_{0.25}\text{Al}_2$  and six for Tb and two for Tm atoms for  $\text{Tm}_{0.25}\text{Tb}_{0.75}\text{Al}_2$  were randomly selected. The total energies and magnetic moments calculated for 20 models with different random placements of six Tm and two Tb atoms for  $\text{Tm}_{0.75}\text{Tb}_{0.25}\text{Al}_2$  were identical within 1.0 meV/cell and 0.02  $\mu_B$ /R atom ( $R = \text{Tb}, \text{Tm}$ ). This indicates that the placement of Tm and Tb atoms has little to no effect on calculated magnetic properties assuming collinear ferromagnetism.

The formation energies of  $\text{Tm}_{0.75}\text{Tb}_{0.25}\text{Al}_2$  and  $\text{Tm}_{0.25}\text{Tb}_{0.75}\text{Al}_2$  calculated from the corresponding total energies of the compounds and their components show negative values indicating that both are stable compounds. The formation energy of  $\text{Tm}_{0.25}\text{Tb}_{0.75}\text{Al}_2$  is lower by 286 meV/Cell when compared to  $\text{Tm}_{0.75}\text{Tb}_{0.25}\text{Al}_2$ , which indicates that  $\text{Tm}_{0.25}\text{Tb}_{0.25}\text{Al}_2$  is energetically more favorable than  $\text{Tm}_{0.75}\text{Tb}_{0.25}\text{Al}_2$ . The calculated equilibrium lattice parameters within LSDA are 7.70 Å and 7.72 Å for  $\text{Tm}_{0.75}\text{Tb}_{0.25}\text{Al}_2$  and  $\text{Tm}_{0.25}\text{Tb}_{0.75}\text{Al}_2$ , respectively. From GGA calculations these



parameters increase to 7.78 Å and 7.80 Å which are in agreement with the experimentally observed values of 7.7974 Å and 7.8425 Å, respectively.

The spin polarized conduction electron (*spd*) density of states (DOS) around the Fermi level for  $\text{Tm}_{0.75}\text{Tb}_{0.25}\text{Al}_2$  and  $\text{Tm}_{0.25}\text{Tb}_{0.75}\text{Al}_2$  compounds have been calculated and shown in Fig. 13a. There is a substantial spin polarization of the *5d* states of  $\text{Tb}^{3+}$  compared to  $\text{Tm}^{3+}$ . This amounts to  $\sim 0.20 \mu_B$  *5d* magnetic moment in Tb but nearly zero ( $\sim 0.02 \mu_B$ ) *5d* magnetic moment in Tm for both  $\text{Tm}_{0.75}\text{Tb}_{0.25}\text{Al}_2$  and  $\text{Tm}_{0.25}\text{Tb}_{0.75}\text{Al}_2$ . The GGA calculations within TB-LMTO and FP-LAPW also show similar values ( $0.22 \mu_B/\text{Tb}$  and  $0.02 \mu_B/\text{Tm}$ ) for *5d* moments. The calculations with LSDA+U approach show slightly higher *5d* moments ( $\sim 0.24 \mu_B$ ) in Tb. As expected, the calculated *s* and *p* moments are negligible. We note that the spin polarization in the *5d* (conduction) electrons is a measure of the indirect *4f-4f* exchange. Because of the higher Tm content, the RKKY exchange is lower in  $\text{Tm}_{0.75}\text{Tb}_{0.25}\text{Al}_2$  when compared to  $\text{Tm}_{0.25}\text{Tb}_{0.75}\text{Al}_2$ . The LSDA+U approach shows *4f* spin moments close to the values ( $6 \mu_B/\text{Tb}$  and  $2 \mu_B/\text{Tm}$ ) predicted from Hund's rule. On the other hand the *4f* orbital moments are  $3.0 \mu_B/\text{Tb}$  and  $5.0 \mu_B/\text{Tm}$ , respectively. This indicates that the orbital moment, which is dominant in Tm, has a substantial contribution in  $\text{Tm}_{0.75}\text{Tb}_{0.25}\text{Al}_2$  compared to  $\text{Tm}_{0.25}\text{Tb}_{0.75}\text{Al}_2$  (Table 1). As noted in previous papers<sup>13,16</sup> the orbital moment contribution is higher in  $\text{Er}_{0.75}\text{Tb}_{0.25}\text{Al}_2$  and  $\text{Er}_{0.75}\text{Dy}_{0.25}\text{Al}_2$  compared to  $\text{Er}_{0.25}\text{Tb}_{0.75}\text{Al}_2$  and  $\text{Er}_{0.25}\text{Dy}_{0.75}\text{Al}_2$ , respectively (Table 1). Because of the orbital moment contribution there is spin orbit coupling of 0.21 eV in Tb and 0.43 eV in Tm.<sup>29</sup> The spin and orbital moment mismatch and the spin orbit coupling

give rise to the competition between spin moments and orbital moments in these compounds.

As shown in Fig. 14, the occupied spin down  $4f$  states of Tm are substantial in  $\text{Tm}_{0.75}\text{Tb}_{0.25}\text{Al}_2$ ; they interact with spin up  $5d$  located near the Fermi level and oppose the interaction between the spin up  $4f$  and spin up  $5d$ . On the other hand, the interaction between the occupied spin down  $4f$  and spin up  $5d$  is weak in  $\text{Tm}_{0.25}\text{Tb}_{0.75}\text{Al}_2$  because of a small spin contribution from Tm, but the interaction between the spin up  $4f$  and  $5d$  is strong because of strong spin moment contribution from Tb (Table I). This results in the anomaly near the Fermi level and supports the first order character of low temperature transition in  $\text{Tm}_{0.75}\text{Tb}_{0.25}\text{Al}_2$  but not in  $\text{Tm}_{0.25}\text{Tb}_{0.75}\text{Al}_2$ . The crystalline electric field alone does not result in the first order phase transition; for example  $\text{TmAl}_2$  has high crystalline electric field effect but does not show first order phase transition.

Figure 13a shows peaks about 0.2 eV wide below the Fermi level in the majority spin direction DOS of  $\text{Tm}_{0.75}\text{Tb}_{0.25}\text{Al}_2$  and  $\text{Tm}_{0.25}\text{Tb}_{0.75}\text{Al}_2$ . The peak is higher in  $\text{Tm}_{0.25}\text{Tb}_{0.75}\text{Al}_2$  than in  $\text{Tm}_{0.75}\text{Tb}_{0.25}\text{Al}_2$ . These peaks are due to  $t_{2g}$  states within  $5d$  states of Tb and Tm. There is another peak located about 0.4 eV above the Fermi level in the majority spin direction of  $\text{Tm}_{0.75}\text{Tb}_{0.25}\text{Al}_2$ . This peak is due to  $e_g$  states. As is seen from the Fig. 13b the crystal field splitting [ $\Delta(t_{2g}-e_g)$ ] in  $\text{Tm}_{0.75}\text{Tb}_{0.25}\text{Al}_2$  is higher compared to  $\text{Tm}_{0.25}\text{Tb}_{0.75}\text{Al}_2$ . On the other hand, the density of states at the Fermi level and at the  $t_{2g}$  peaks are higher with negligible  $e_g$  states in  $\text{Tm}_{0.25}\text{Tb}_{0.75}\text{Al}_2$  (Fig. 13a) compared to  $\text{Tm}_{0.75}\text{Tb}_{0.25}\text{Al}_2$  indicating dominant  $5d$  spin polarization leading to significant spin

exchange interactions in  $\text{Tm}_{0.25}\text{Tb}_{0.75}\text{Al}_2$  (Fig. 15). The crystal field splitting  $[\Delta(t_{2g}-e_g)]$  was also visible in  $\text{Er}_{0.75}\text{Tb}_{0.25}\text{Al}_2$  and  $\text{Er}_{0.75}\text{Dy}_{0.25}\text{Al}_2$  but not discussed in earlier papers.<sup>13,16</sup> Below we discuss how  $t_{2g} - e_g$  develops in these compounds.

In order to understand how the  $t_{2g} - e_g$  separations in the  $5d$  states are developed in  $\text{Tm}_{0.75}\text{Tb}_{0.25}\text{Al}_2$ ,  $\text{Er}_{0.75}\text{Tb}_{0.25}\text{Al}_2$ , and  $\text{Er}_{0.75}\text{Dy}_{0.25}\text{Al}_2$  we have plotted the majority spin direction conduction electron (*spd*) DOS of pure  $\text{TbAl}_2$ ,  $\text{DyAl}_2$ ,  $\text{ErAl}_2$  and  $\text{TmAl}_2$  (see Fig. 16a). The peak at the Fermi level shifts to higher energy with increasing atomic number in the series  $\text{TbAl}_2 \rightarrow \text{DyAl}_2 \rightarrow \text{ErAl}_2 \rightarrow \text{TmAl}_2$  (Fig. 16b). The magnitude of the peak decreases significantly in  $\text{ErAl}_2$  and  $\text{TmAl}_2$ . When the ternary compounds are formed, depending upon the concentrations of the lanthanide metals, the DOS peaks at the Fermi level due to either Tb or Dy act as  $t_{2g}$  states while those due to Er or Tm act as  $e_g$  states. At large concentrations of Tb or Dy the  $e_g$  states are weak and therefore the states near the Fermi level act as the  $t_{2g}$  states. In this case, since the spin moment due to Tb or Dy is higher than the orbital moment, the spin exchange interactions are more effective than the spin orbit and crystalline electric field interactions. On the other hand, with larger concentrations of Er or Tm the  $e_g$  states above the Fermi level are strong and the  $t_{2g}$  states at the Fermi level are also significant due to the high DOS peak coming from Tb or Dy. Therefore, the separation of the  $t_{2g}$  and  $e_g$  states developed due to Er or Tm content competes with the spin polarization at the Fermi level due to Tb or Dy content which may ultimately lead to the low temperature anomalies observed in  $\text{Tm}_{0.75}\text{Tb}_{0.25}\text{Al}_2$ ,  $\text{Er}_{0.75}\text{Tb}_{0.25}\text{Al}_2$ , and  $\text{Er}_{0.75}\text{Dy}_{0.25}\text{Al}_2$ .

In addition to the spin orbit coupling and crystal field effects discussed above, we have to consider higher order interactions such as quadrupolar interactions which may play a pivotal role because the  $4f$  charges of  $\text{Tm}^{3+}$  and  $\text{Tb}^{3+}$  ions are non spherical; they are prolate and oblate, respectively. The second order Stevens' coefficients ( $\alpha_2$ ) are negative for Tb and positive for Tm although they are equal in magnitude (Table II).<sup>15</sup> The fourth order and sixth order Stevens' coefficients for Tb and Tm have same signs but these coefficients are smaller compared to the second order ones.<sup>15</sup> Although these higher order Stevens' coefficients contribute to the higher order magnetocrystalline anisotropy, the substantial change in the shape of the charge densities of different rare earths is due to the second order Stevens' coefficients.

The perturbed charge densities give rise to the quadrupolar moment,

$$\frac{Q_2}{a_0^2} = \frac{\alpha_J \langle r^2 \rangle_{4f} (2J^2 - J)}{a_0^2}. \text{ The estimated quadrupolar moments from point charge model}$$

for Tb and Tm are -0.505 and 0.427.<sup>30,5</sup> The higher order moments of Tb and Tm are with same sign (Table II) and may contribute only to the higher order magnetocrystalline anisotropy. The approximate anisotropy energy may be expressed in terms of

magnetization angle  $\theta$  [ $E_a = \frac{1}{2} Q_2 A_2^0 (3 \cos^2 \theta - 1)$ ] and the lowest order uniaxial

anisotropic constant ( $K_1 = -\frac{3}{2V_R} Q_2 A_2^0$ ) is expressed in terms of the shape of the  $4f$  shell,

described by  $Q_2$  and the crystal field environment, described by  $A_2^0$ . Here,  $A_2^0$  is the second order uniaxial crystal field parameter and  $V_R$  is the crystal volume per rare earth

atom. It is interesting to note that although the values of  $A_2^0$  for rare earths differ slightly, they have same sign<sup>31</sup> indicating that the uniaxial anisotropy in rare earth compounds depends largely on the sign of the quadrupolar moment  $Q_2$  but not on the sign of  $A_2^0$ . As shown in Fig. 15 in  $\text{Tm}_{1-x}\text{Tb}_x\text{Al}_2$  the spin exchange interactions are dominant at larger concentrations of Tb or Dy, while the anisotropy which originates from the quadrupolar moments or Stevens' second order coefficients through the orbital moments will be effective only in the compounds with the higher concentrations of Tm or Er.

Therefore, overall it may be concluded that the magnetic exchange, spin orbit coupling, crystal field, and quadrupolar interactions compete with each other at low temperatures and this competition could lead to the low temperature first order like anomaly seen in  $\text{Tm}_{0.75}\text{Tb}_{0.25}\text{Al}_2$  as well as in  $\text{Er}_{0.75}\text{Tb}_{0.25}\text{Al}_2$  and  $\text{Er}_{0.75}\text{Dy}_{0.25}\text{Al}_2$ . On the other hand the spin moment contribution in  $\text{Tm}_{0.25}\text{Tb}_{0.75}\text{Al}_2$  is so strong that the spin exchange interaction dominates over the orbital contribution as in the case of pure  $\text{TbAl}_2$  and  $\text{DyAl}_2$  and therefore the low temperature first order type anomaly is not seen in  $\text{Tm}_{0.25}\text{Tb}_{0.75}\text{Al}_2$ ,  $\text{Er}_{0.25}\text{Tb}_{0.75}\text{Al}_2$  and  $\text{Er}_{0.25}\text{Dy}_{0.75}\text{Al}_2$ .

## Conclusions

By using the second order Stevens' factors of  $\text{Tm}^{3+}$  and  $\text{Tb}^{3+}$  ions, prediction was made that first order like anomalies exist in the  $\text{Tm}_{1-x}\text{Tb}_x\text{Al}_2$  alloys. The anomalies observed in the dc and ac magnetization, and the heat capacity data of  $\text{Tm}_{1-x}\text{Tb}_x\text{Al}_2$  are similar to

those observed in  $\text{Er}_{1-x}\text{Dy}_x\text{Al}_2$  and  $\text{Er}_{1-x}\text{Tb}_x\text{Al}_2$ . As predicted, the results available so far, strongly suggest that the multiple magnetic ordering phenomena observed earlier in the  $\text{Er}_{1-x}\text{Dy}_x\text{Al}_2$  and  $\text{Er}_{1-x}\text{Tb}_x\text{Al}_2$  alloys are not only restricted to Er based  $\text{RAl}_2$  alloys, and appear to be present in a broader range of compounds. Most interestingly, the critical concentration around which the multiple magnetic ordering is observed in all the  $\text{Er}_{1-x}\text{Dy}_x\text{Al}_2$ ,  $\text{Er}_{1-x}\text{Tb}_x\text{Al}_2$ , and  $\text{Tm}_{1-x}\text{Tb}_x\text{Al}_2$  alloys is always  $x = 0.25$ . Magnetic susceptibility and heat capacity measurements show the existence of unusual first order-like anomaly in  $\text{Tm}_{0.75}\text{Tb}_{0.25}\text{Al}_2$  alloy at  $\sim 7$  K. Low temperature XRD measurements show that the first order like transition is not accompanied by any crystal structure change, and volume discontinuity that should accompany the first order phase transition is smaller than the error limits of the XRD technique (usually 20-40 ppm). The obtained experimental results are also supported by the results of first principles calculations that show anomalies in the DOS at the Fermi level. The observed behavior strongly suggests that the Stevens' coefficients may be used as a powerful tool to predict magnetic transitions in pseudo binary  $\text{R}_{1-x}\text{R}'_x\text{Al}_2$  alloys, and potentially, in other mixed lanthanide alloys.

## Acknowledgement

This work was supported by the U.S. Department of Energy, Office of Basic Energy Science, Division of Materials Sciences and Engineering. The research was performed at the Ames Laboratory. Ames Laboratory is operated for the U.S. Department of Energy by Iowa State University under Contract No. DE-AC02-07CH11358.

## References

---

- <sup>1</sup> H. J. Williams, J. H. Wernick, E. A. Nesbitt, and R. C. Sherwood, J. Phys. Soc. Japan **17**, suppl. B-I, 91 (1962).
- <sup>2</sup> N. Nereson, C. Olsen, and G. Arnold, J. Appl. Phys. **37**, 4575 (1966).
- <sup>3</sup> N. Nereson, C. Olsen, and G. Arnold, J. Appl. Phys. **39**, 4605 (1968).
- <sup>4</sup> N. Kaplan, E. Dormann, K. H. J. Buschow, and D. Lebenbaum, Phys. Rev. B **7**, 40 (1973).
- <sup>5</sup> H. J. Purwins and A. Leson, Adv. Phys. **39**, 309 (1990).
- <sup>6</sup> H. Adachi and H. Ino, Nature (London) **401**, 148 (1999).
- <sup>7</sup> K. A. Gschneidner, Jr., H. Takeya, J. O. Moorman, and V. K. Pecharsky, Appl. Phys. Lett. **64**, 253 (1994).
- <sup>8</sup> K. A. Gschneidner, Jr., V. K. Pecharsky, and S. K. Malik, Adv. Cryog. Eng. **42**, 475 (1996).
- <sup>9</sup> P. D. Kulkarni, A. Thamizhavel, V. C. Rakhecha, A. K. Nigam, P. L. Paulose, S. Ramakrishnan and A. K. Grover, Euro. Phys. Lett., **86**, 47003 (2009).
- <sup>10</sup> A. L. Lima, K. A. Gschneidner, Jr., V. K. Pecharsky, and A. O. Pecharsky, Phys. Rev. B **68**, 134409 (2003).
- <sup>11</sup> R. Nirmala, Ya. Mudryk, V. K. Pecharsky and K. A. Gschneidner, Jr., Phys. Rev. B **76**, 014407 (2007).
- <sup>12</sup> Mahmud Khan, K. A. Gschneidner and V. K. Pecharsky , Jr., Phys. Rev. B **80**, 224408 (2009).

- 
- <sup>13</sup> Mahmud Khan, Ya. Mudryk, D. Paudyal, K. A. Gschneidner, Jr. and V. K. Pecharsky, Phys. Rev. B **82**, 064421 (2010).
- <sup>14</sup> P.G. de Gennes, Compt. Rend. **247**, 1836 (1958).
- <sup>15</sup> K. W. H. Stevens, Proc. Phys. Soc. LXV, **A65**, 209-215 (1952).
- <sup>16</sup> R. Nirmala, D. Paudyal, V. K. Pecharsky, and K. A. Gschneidner, Jr., J. Appl. Phys., **107**, 09A723 (2010).
- <sup>17</sup> Materials Preparation Center, Ames Laboratory US-DOE, Ames, IA, USA, [www.mpc.ameslab.gov](http://www.mpc.ameslab.gov).
- <sup>18</sup> A. P. Holm, V. K. Pecharsky, K. A. Gschneidner, Jr., R. Rink, and M. N. Jirmanus Rev. Sci. Instrum. **75**, 1081 (2004).
- <sup>19</sup> Ya. Mudryk, A. P. Holm, K. A. Gschneidner, Jr., and V. K. Pecharsky, Phys. Rev. B **72**, 064442 (2005).
- <sup>20</sup> B. Hunter, Rietica-A Visual Rietveld Program, International Union of Crystallography Commission on Powder Diffraction Newsletter No. 20, (Summer, 1998) <http://www.rietica.org>.
- <sup>21</sup> I.R. Harris, R.C. Mansey and G.V. Raynor J Less-Common Metals **9**, 270 (1965).
- <sup>22</sup> K.A. Gschneidner Jr., Ya. Mudryk, A.T. Becker, J.L. Larson, CALPHAD **33**, 8 (2009).
- <sup>23</sup> V. K. Pecharsky, J. O. Moorman, and K. A. Gschneidner, Jr., Rev. Sci. Instrum. **68**, 4196 (1997).
- <sup>24</sup> H. J. Williams, J. H. Wernick, E. A. Nesbitt, and R. C. Sherwood, J. Phys. Soc. Jpn. **17-B1**, 91 (1962).



- 
- <sup>25</sup> A.F. Deutz, H.B. Brom, W.J. Huiskamp, L.J. de Jongh and K.H.J. Buschow. Solid State Commun. **68**, 803 (1988).
- <sup>26</sup> O K Andersen and O Jepsen, Phys. Rev. Lett. **53**, 2571 (1984).
- <sup>27</sup> V I Anisimov, F Aryasetiawan, and A I Liechtenstein, J. Phys.: Condens. Matter **9**, 767 (1997).
- <sup>28</sup> B N Harmon, V P Antropov, A I Liechtenstein, I V Solovyev, and V I Anisimov, J. Phys. Chem. Solids **56**, 1521 (1995).
- <sup>29</sup> S. Lebegue, A. Svane, M. I. Katsnelson, A. I. Lichtenstein, and O. Eriksson, J. Phys.: Condens. Matter **18**, 6329 (2006).
- <sup>30</sup> R. Skomski, in *Simple Models of Magnetism* (Oxford, University Press, 2006) Chap. 3, p.94 and the references therein.
- <sup>31</sup> F. Welsch, M. Fahnle, and P.J. Jensen, J. Phys. Condens. Matter **17**, 2061 (2005).

## Table Captions

Table I. The spin and orbital  $4f$  moments per formula unit. The orbital moments are higher than the spin moments in 75-25 compounds. The spin moments are higher than the orbital moments in 25-75 compounds except  $\text{Er}_{0.25}\text{Dy}_{0.75}\text{Al}_2$ . Although the orbital moment is higher than the spin moment in  $\text{Er}_{0.25}\text{Dy}_{0.75}\text{Al}_2$  the spin moment of  $\text{Er}_{0.25}\text{Dy}_{0.75}\text{Al}_2$  is higher than that of the spin moment of  $\text{Er}_{0.75}\text{Dy}_{0.25}\text{Al}_2$ .

TABLE II. The number of  $4f$  electrons,  $n_i$ , the total angular momentum quantum number,  $J_i$ , the Stevens' second order coefficient,  $\alpha_i$ , and higher order moments,  $Q_i/a_0^i$ , of tripositive Tb and Tm ions in their ground states.

## Figure Captions

FIG. 1 (Color online). Observed (symbols) and calculated (line drawn through the symbols) room temperature X-ray powder diffraction pattern of  $\text{Tm}_{0.75}\text{Tb}_{0.25}\text{Al}_2$ . The difference  $I_{\text{obs}} - I_{\text{calc}}$  is shown at the bottom of the plot. Vertical bars under the patterns indicate calculated positions of Bragg peaks of  $\text{Tm}_{0.75}\text{Tb}_{0.25}\text{Al}_2$ . The inset shows the lattice parameter as a function of Tb concentration (x). The lattice parameter of  $\text{TmAl}_2$  (the lowest point in the figure) was taken from reference 21.

FIG. 2 (Color online). Temperature dependencies of dc magnetization of  $\text{Tm}_{0.75}\text{Tb}_{0.25}\text{Al}_2$  measured in an applied field of 100 Oe under ZFC, FCC, and FCW conditions. Inset (a) shows the details of the low temperature region around the transition, and inset (b) shows the derivatives of the ZFC and FCC data.

FIG. 3 (Color online). Temperature dependencies of dc magnetization of  $\text{Tm}_{0.75}\text{Tb}_{0.25}\text{Al}_2$  measured in an applied field of 1000 Oe under ZFC, FCC, and FCW conditions. The inset shows the temperature dependence of the inverse susceptibility ( $H/M$ ) for a field of 1000 Oe.

FIG. 4 (Color online). Field dependence of magnetization of  $\text{Tm}_{0.75}\text{Tb}_{0.25}\text{Al}_2$  measured at 2 K. The inset shows the behavior of the data near  $H = 0$ .

FIG. 5 (Color online). (a) Temperature dependence of real component of the ac magnetic susceptibility ( $\chi'$ ) of  $\text{Tm}_{0.75}\text{Tb}_{0.25}\text{Al}_2$  measured in an ac field of 5 Oe and frequencies from 1 Hz to 1000 Hz. Inset (a) shows the details of the low temperature region around the transition. (b) The imaginary components ( $\chi''$ ) of the ac magnetic susceptibility of  $\text{Tm}_{0.75}\text{Tb}_{0.25}\text{Al}_2$ .

FIG. 6 (Color online). The zero magnetic field heat capacity and the 100 Oe field  $M(T)$  data of  $\text{Tm}_{0.75}\text{Tb}_{0.25}\text{Al}_2$  as a function of temperature.

FIG. 7 (Color online). The heat capacities of  $\text{Tm}_{0.75}\text{Tb}_{0.25}\text{Al}_2$  as a function of temperature measured in different magnetic fields. The inset clarifies the behavior around the low temperature anomaly.

FIG. 8. The lattice parameter  $a$  of  $\text{Tm}_{0.75}\text{Tb}_{0.25}\text{Al}_2$  as a function of temperature.

FIG. 9 (Color online). Temperature dependencies of dc magnetization of  $\text{Tm}_{0.25}\text{Tb}_{0.75}\text{Al}_2$  measured in an applied field of 100 Oe under ZFC, FCC, and FCW conditions. The upper inset shows the  $M(T)$  data obtained under same condition for  $\text{TbAl}_2$ , and the lower inset shows the dependence of  $T_C$  on Tb concentration ( $x$ ). The Curie temperature for  $\text{TmAl}_2$  was taken from Deutz et al.<sup>25</sup>

FIG. 10 (Color online). Temperature dependencies of dc magnetization of  $\text{Tm}_{0.25}\text{Tb}_{0.75}\text{Al}_2$  measured in an applied field of 1000 Oe under ZFC, FCC, and FCW conditions. The

inset shows the temperature dependence of the inverse susceptibility ( $H/M$ ) for a field of 1000 Oe.

FIG. 11 (Color online). Temperature dependence of real component of the ac magnetic susceptibility of  $\text{Tm}_{0.25}\text{Tb}_{0.75}\text{Al}_2$  measured in an ac field of 5 Oe and frequencies from 1 Hz to 1000 Hz. The inset of Fig. 8 shows the imaginary component of the ac magnetic susceptibility of  $\text{Tm}_{0.25}\text{Tb}_{0.75}\text{Al}_2$ .

FIG. 12 (Color online). Zero magnetic field heat capacity data of  $\text{Tm}_{0.25}\text{Tb}_{0.75}\text{Al}_2$  measured as a function of temperature.

FIG. 13 (Color online). (a) The majority and minority spin conduction electron density of states of  $\text{Tm}_{0.25}\text{Tb}_{0.75}\text{Al}_2$  (dashed lines) and  $\text{Tm}_{0.75}\text{Tb}_{0.25}\text{Al}_2$  (solid lines) around the Fermi level. (b) The  $t_{2g} - e_g$  separation and the density of states at the Fermi level as a function of Tb concentration ( $x$ ).

Fig. 14. The density of states contributions of Tb (4f) and Tm (4f) electrons in  $\text{Tm}_{0.75}\text{Tb}_{0.25}\text{Al}_2$ . The 4f spin up density of states are split in both Tb and Tm while the occupied spin down density of states are split in Tm but not in Tb.

FIG. 15 (Color online). The exchange interactions and the quadrupolar moment as a function of Tb concentration ( $x$ ) in  $\text{Tm}_{1-x}\text{Tb}_x\text{Al}_2$ .

FIG. 16 (Color online). (a) The majority spin direction conduction electron DOS of  $\text{TbAl}_2$ ,  $\text{DyAl}_2$ ,  $\text{ErAl}_2$  and  $\text{TmAl}_2$ . (b) The position of DOS peak relative to the Fermi level as a function of atomic number of R in  $\text{RAl}_2$ .

Table I. The spin and orbital 4*f* moments per formula unit. The orbital moments are higher than the spin moments in 75-25 compounds. The spin moments are higher than the orbital moments in 25-75 compounds except Er<sub>0.25</sub>Dy<sub>0.75</sub>Al<sub>2</sub>. Although the orbital moment is higher than the spin moment in Er<sub>0.25</sub>Dy<sub>0.75</sub>Al<sub>2</sub> the spin moment of Er<sub>0.25</sub>Dy<sub>0.75</sub>Al<sub>2</sub> is higher than that of the spin moment of Er<sub>0.75</sub>Dy<sub>0.25</sub>Al<sub>2</sub>.

Compound	4 <i>f</i> spin moment	4 <i>f</i> orbital moment
Tm <sub>0.75</sub> Tb <sub>0.25</sub> Al <sub>2</sub>	3.00	4.50
Er <sub>0.75</sub> Tb <sub>0.25</sub> Al <sub>2</sub>	3.75	5.25
Er <sub>0.75</sub> Dy <sub>0.25</sub> Al <sub>2</sub>	3.50	5.75
Tm <sub>0.25</sub> Tb <sub>0.75</sub> Al <sub>2</sub>	5.00	3.50
Er <sub>0.25</sub> Tb <sub>0.75</sub> Al <sub>2</sub>	5.25	3.75
Er <sub>0.25</sub> Dy <sub>0.75</sub> Al <sub>2</sub>	4.50	5.25

TABLE II. The number of  $4f$  electrons,  $n_i$ , the total angular momentum quantum number,  $J_i$ , the Stevens' second order coefficient,  $\alpha_i$ , and higher order moments,  $Q_i/a_0^i$ , of tripositive Tb and Tm ions in their ground states.

	n	J	$\alpha_2$	$Q_2/a_0^2$	$Q_4/a_0^4$	$Q_6/a_0^6$
Tb	8	6	-0.0101	-0.505	1.047	-1.082
Tm	12	6	0.0101	0.427	0.999	-4.201



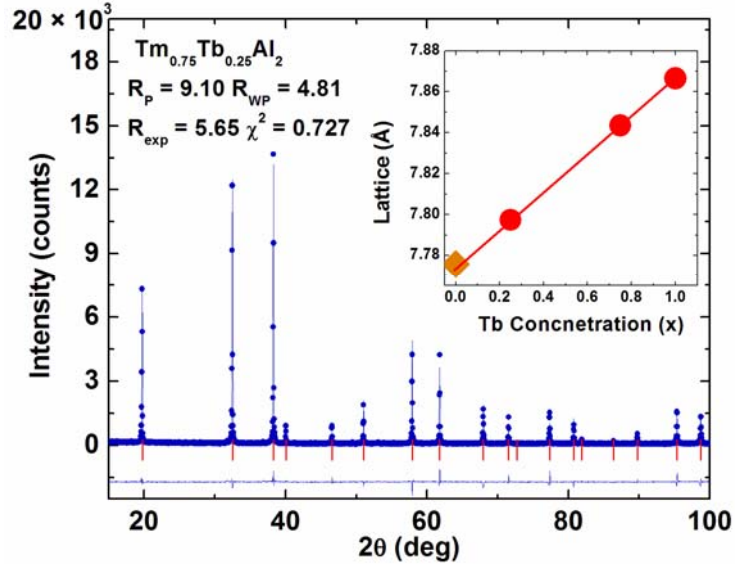


FIG. 1 (Color online). Observed (symbols) and calculated (line drawn through the symbols) room temperature X-ray powder diffraction pattern of  $\text{Tm}_{0.75}\text{Tb}_{0.25}\text{Al}_2$ . The difference  $I_{\text{obs}} - I_{\text{calc}}$  is shown at the bottom of the plot. Vertical bars under the patterns indicate calculated positions of Bragg peaks of  $\text{Tm}_{0.75}\text{Tb}_{0.25}\text{Al}_2$ . The inset shows the lattice parameter as a function of Tb concentration (x). The lattice parameter of  $\text{TmAl}_2$  (the lowest point in the figure) was taken from reference 21.

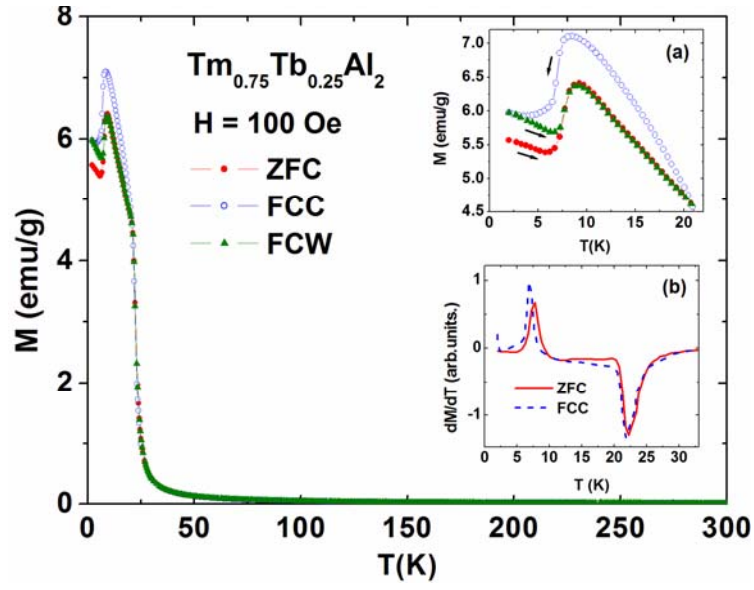


FIG. 2 (Color online). Temperature dependencies of dc magnetization of  $\text{Tm}_{0.75}\text{Tb}_{0.25}\text{Al}_2$  measured in an applied field of 100 Oe under ZFC, FCC, and FCW conditions. Inset (a) shows the details of the low temperature region around the transition, and inset (b) shows the derivatives of the ZFC and FCC data.

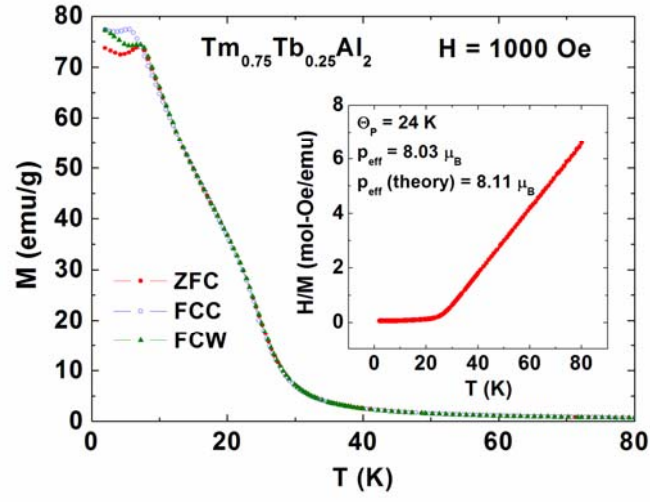


FIG. 3 (Color online). Temperature dependencies of dc magnetization of  $\text{Tm}_{0.75}\text{Tb}_{0.25}\text{Al}_2$  measured in an applied field of 1000 Oe under ZFC, FCC, and FCW conditions. The inset shows the temperature dependence of the inverse susceptibility ( $H/M$ ) for a field of 1000 Oe.

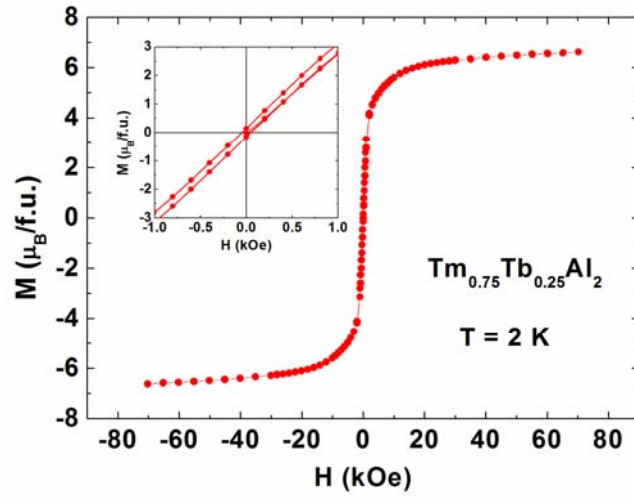


FIG. 4 (Color online). Field dependence of magnetization of  $\text{Tm}_{0.75}\text{Tb}_{0.25}\text{Al}_2$  measured at 2 K. The inset shows the behavior of the data near  $H = 0$ .

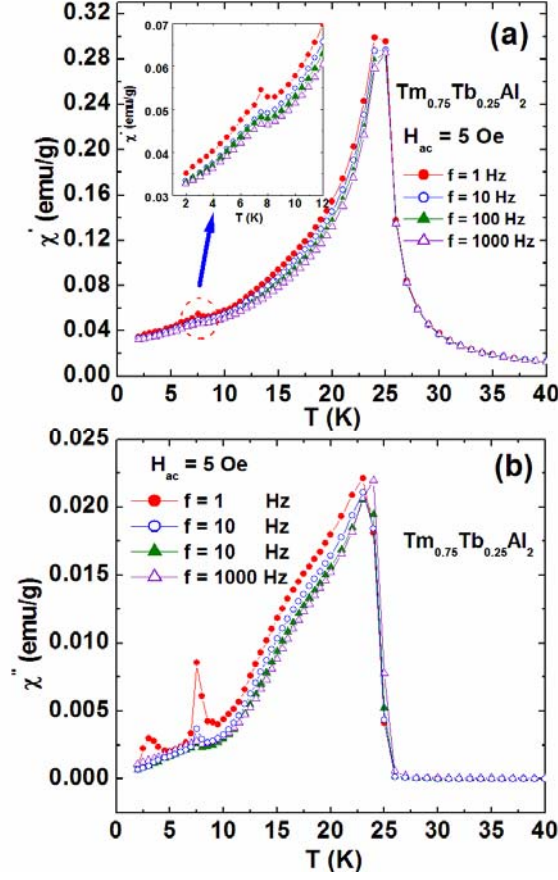


FIG. 5 (Color online). (a) Temperature dependence of real component of the ac magnetic susceptibility ( $\chi'$ ) of  $\text{Tm}_{0.75}\text{Tb}_{0.25}\text{Al}_2$  measured in an ac field of 5 Oe and frequencies from 1 Hz to 1000 Hz. Inset (a) shows the details of the low temperature region around the transition. (b) The imaginary components ( $\chi''$ ) of the ac magnetic susceptibility of  $\text{Tm}_{0.75}\text{Tb}_{0.25}\text{Al}_2$ .

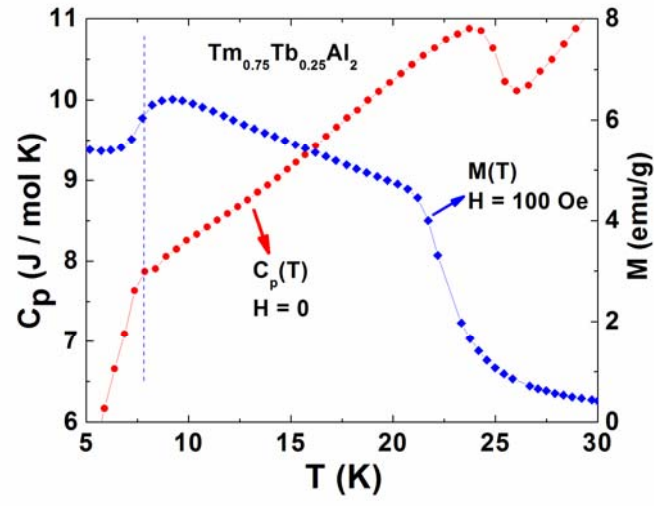


FIG. 6 (Color online). The zero magnetic field heat capacity and the 100 Oe field  $M(T)$  data of  $\text{Tm}_{0.75}\text{Tb}_{0.25}\text{Al}_2$  as a function of temperature.

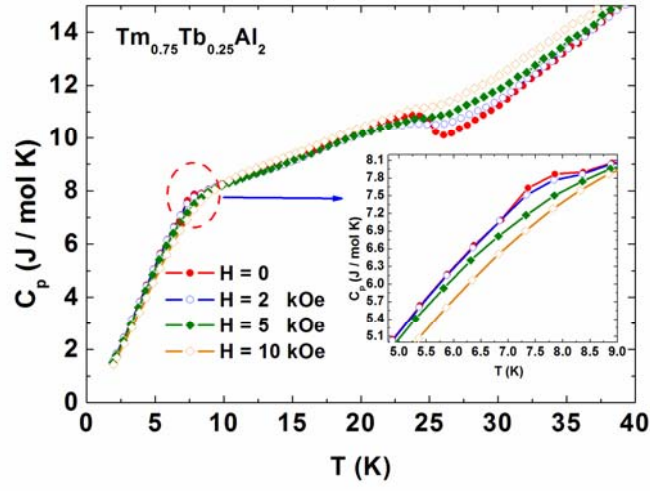


FIG. 7 (Color online). The heat capacities of  $\text{Tm}_{0.75}\text{Tb}_{0.25}\text{Al}_2$  as a function of temperature measured in different magnetic fields. The inset clarifies the behavior around the low temperature anomaly.

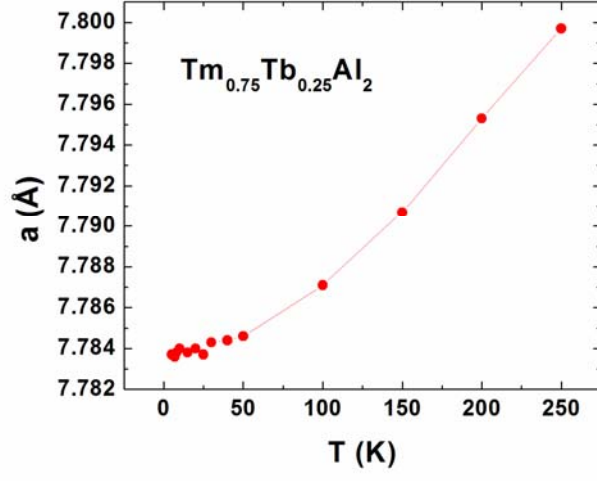


FIG. 8. The lattice parameter  $a$  of  $\text{Tm}_{0.75}\text{Tb}_{0.25}\text{Al}_2$  as a function of temperature.



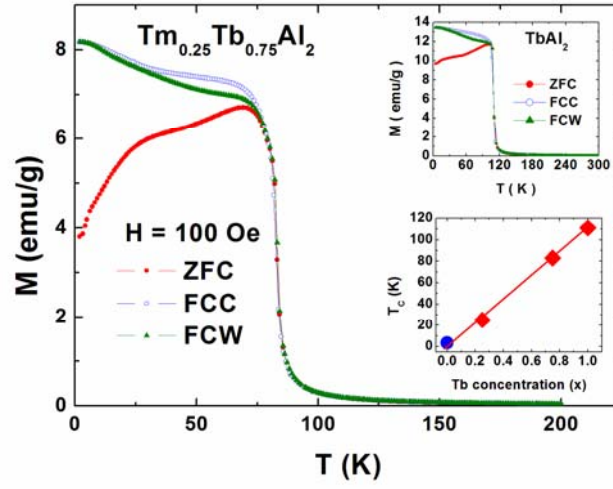


FIG. 9 (Color online). Temperature dependencies of dc magnetization of  $\text{Tm}_{0.25}\text{Tb}_{0.75}\text{Al}_2$  measured in an applied field of 100 Oe under ZFC, FCC, and FCW conditions. The upper inset shows the  $M(T)$  data obtained under same condition for  $\text{TbAl}_2$ , and the lower inset shows the dependence of  $T_C$  on Tb concentration ( $x$ ). The Curie temperature for  $\text{TmAl}_2$  was taken from Deutz et al.<sup>25</sup>

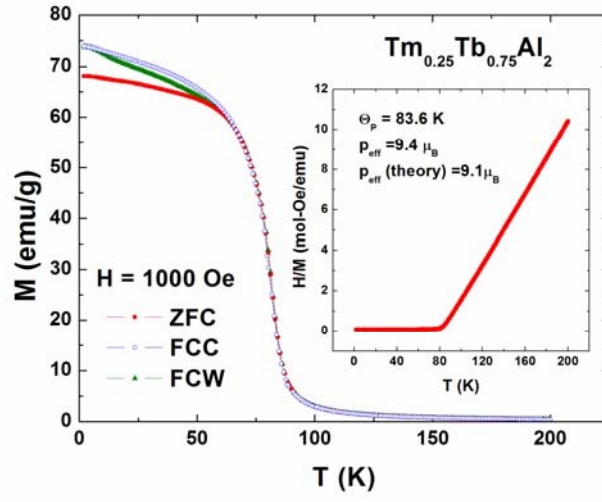


FIG. 10 (Color online). Temperature dependencies of dc magnetization of  $\text{Tm}_{0.25}\text{Tb}_{0.75}\text{Al}_2$  measured in an applied field of 1000 Oe under ZFC, FCC, and FCW conditions. The inset shows the temperature dependence of the inverse susceptibility ( $H/M$ ) for a field of 1000 Oe.

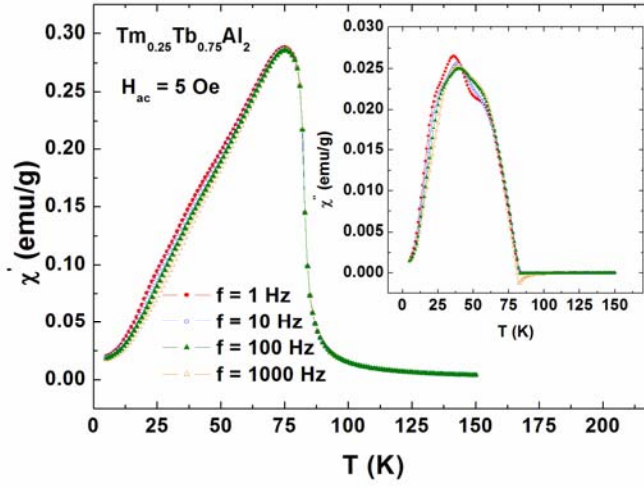


FIG. 11 (Color online). Temperature dependence of real component of the ac magnetic susceptibility of  $\text{Tm}_{0.25}\text{Tb}_{0.75}\text{Al}_2$  measured in an ac field of 5 Oe and frequencies from 1 Hz to 1000 Hz. The inset of Fig. 8 shows the imaginary component of the ac magnetic susceptibility of  $\text{Tm}_{0.25}\text{Tb}_{0.75}\text{Al}_2$ .

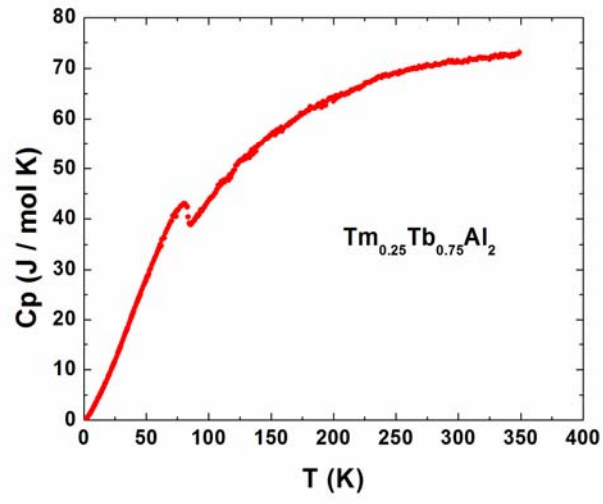


FIG. 12 (Color online). Zero magnetic field heat capacity data of  $\text{Tm}_{0.25}\text{Tb}_{0.75}\text{Al}_2$  measured as a function of temperature.

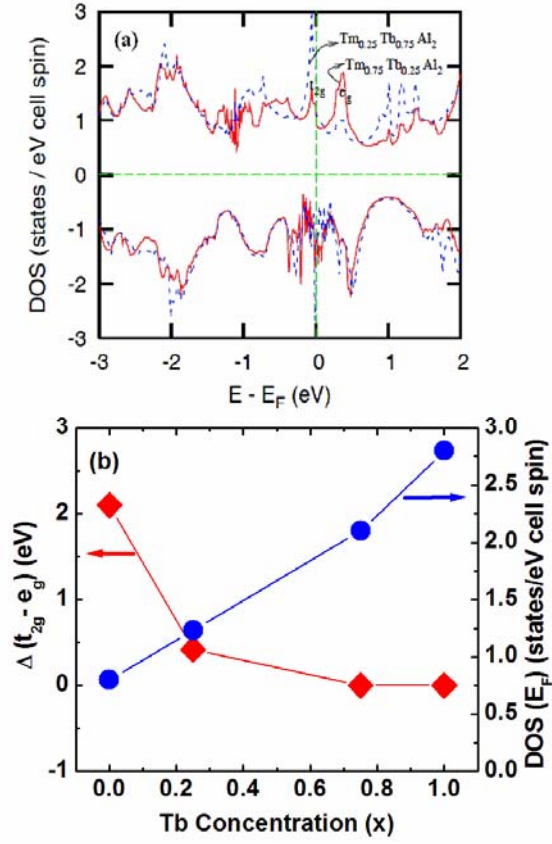


FIG. 13 (Color online). (a) The majority and minority spin conduction electron density of states of  $\text{Tm}_{0.25}\text{Tb}_{0.75}\text{Al}_2$  (dashed lines) and  $\text{Tm}_{0.75}\text{Tb}_{0.25}\text{Al}_2$  (solid lines) around the Fermi level. (b) The  $t_{2g} - e_g$  separation and the density of states at the Fermi level as a function of Tb concentration ( $x$ ).

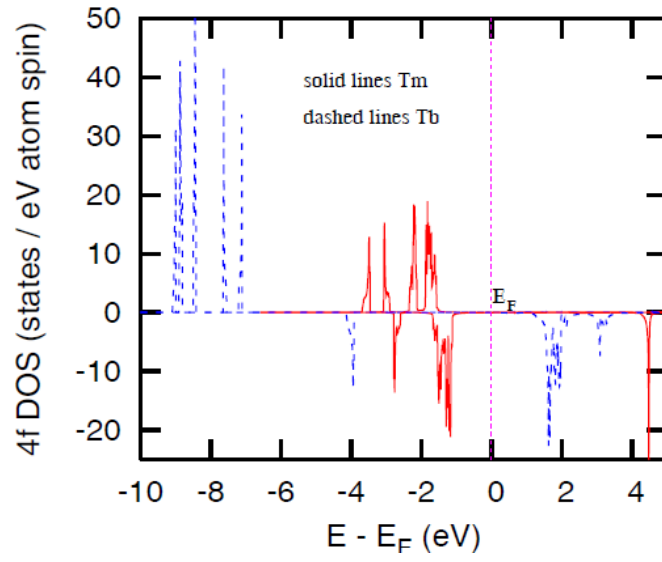


Fig. 14. The density of states contributions of Tb (4f) and Tm (4f) electrons in  $\text{Tm}_{0.75}\text{Tb}_{0.25}\text{Al}_2$ . The 4f spin up density of states are split in both Tb and Tm while the occupied spin down density of states are split in Tm but not in Tb.

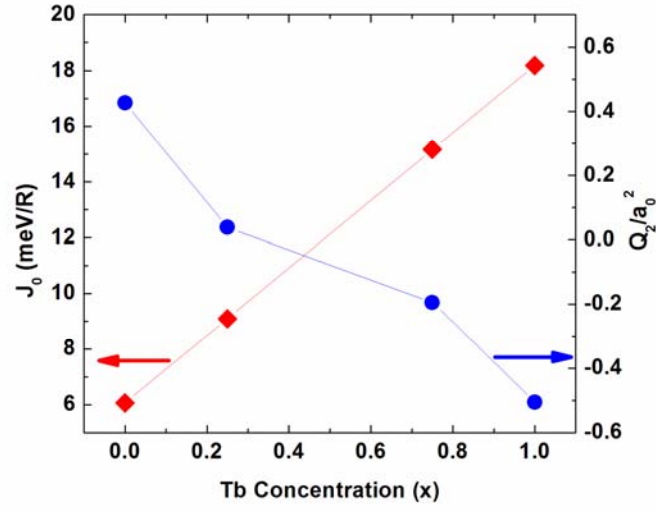


FIG. 15 (Color online). The exchange interactions and the quadrupolar moment as a function of Tb concentration ( $x$ ) in  $\text{Tm}_{1-x}\text{Tb}_x\text{Al}_2$ .

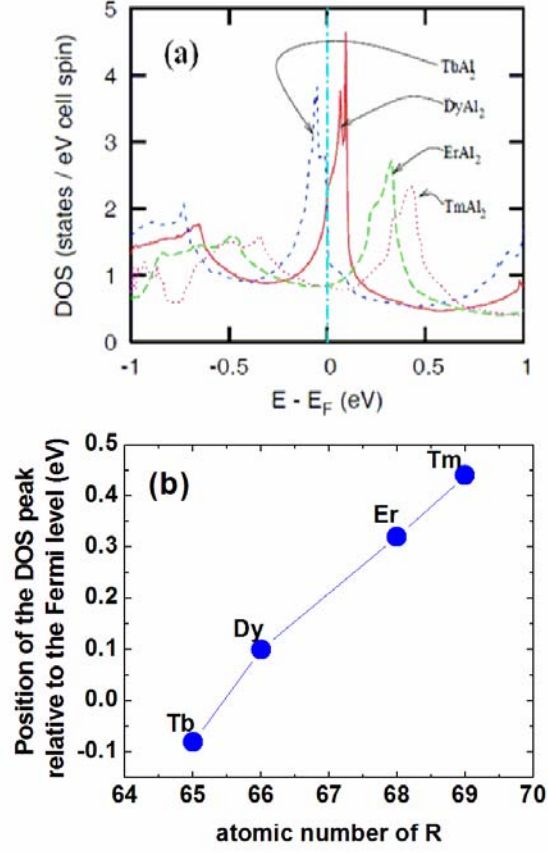


FIG. 16 (Color online). (a) The majority spin direction conduction electron DOS of TbAl<sub>2</sub>, DyAl<sub>2</sub>, ErAl<sub>2</sub> and TmAl<sub>2</sub>. (b) The position of DOS peak relative to the Fermi level as a function of atomic number of R in RAl<sub>2</sub>.